Monthly Notices
of the
ROYAL ASTRONOMICAL SOCIETY

Mon. Not. R. Astron. Soc. **406,** 1659–1674 (2010) doi:10.1111/j.1365-2966.2010.16810.x

A comparison between grid and particle methods on the statistics of driven, supersonic, isothermal turbulence

Daniel J. Price[1⋆] and Christoph Federrath[1,2,3]

[1]*Centre for Stellar and Planetary Astrophysics, School of Mathematical Sciences, Monash University, Clayton, Vic 3168, Australia*
[2]*Zentrum für Astronomie der Universität Heidelberg, Institut für Theoretische Astrophysik, Albert-Ueberle-Str. 2, D-69120 Heidelberg, Germany*
[3]*Max-Planck-Institute for Astronomy, Königstuhl 17, D-69117 Heidelberg, Germany*

Accepted 2010 April 8. Received 2010 April 5; in original form 2009 September 28

ABSTRACT

We compare the statistics of driven, supersonic turbulence at a high Mach number using FLASH, a widely used Eulerian grid-based code, and PHANTOM, a Lagrangian smoothed particle hydrodynamics (SPH) code at resolutions of up to 512^3 in both grid cells *and* SPH particles. We find excellent agreement between codes on the basic statistical properties: a slope of $k^{-1.95}$ in the velocity power spectrum for hydrodynamic, Mach 10 turbulence, evidence in both codes for a Kolmogorov-like slope of $k^{-5/3}$ in the variable $\rho^{1/3}\boldsymbol{v}$ as suggested by Kritsuk et al. and a lognormal probability distribution function (PDF) with a width that scales with the Mach number and proportionality constant $b = 0.33$–0.5 in the density variance–Mach number relation. The measured structure function slopes are not converged in either code at 512^3 elements.

We find that for measuring volumetric statistics such as the power spectrum slope and structure function scaling, SPH and grid codes give roughly comparable results when the number of SPH particles is approximately equal to the number of grid cells. In particular, to accurately measure the power spectrum slope in the inertial range, in the absence of sub-grid turbulence models, requires at least 512^3 computational elements in either code. On the other hand the SPH code was found to be better at resolving dense structures, giving maximum densities at a resolution of 128^3 particles that were similar to the maximum densities resolved in the grid code at 512^3 cells, reflected also in the high density tail of the PDF. We find SPH to be more dissipative at comparable numbers of computational elements in statistics of the velocity field, but correspondingly less dissipative than the grid code in the statistics of density-weighted quantities such as $\rho^{1/3}\boldsymbol{v}$.

For SPH simulations of high Mach number turbulence, we find it important to use sufficient non-linear β-viscosity in order to prevent particle interpenetration in shocks (we require $\beta_{\rm visc} = 4$ instead of the widely used default value, $\beta_{\rm visc} = 2$).

Key words: hydrodynamics – shock waves – turbulence – methods: numerical – stars: formation – ISM: general.

1 INTRODUCTION

Dense interstellar molecular clouds are ubiquitously observed to have non-thermal linewidths implying supersonic internal motions (Zuckerman & Evans 1974). Furthermore, the amplitude of such motions increases with spatial scale in a manner reminiscent of turbulent flows in the laboratory (Larson 1981; Solomon et al. 1987; Heyer & Brunt 2004). Understanding the nature and origin of such 'supersonic turbulence' is therefore key – perhaps *the* key – to understanding star formation (Elmegreen & Scalo 2004; Mac Low & Klessen 2004; McKee & Ostriker 2007). Turbulence provides a natural explanation for the clustered and hierarchical nature of star formation (Elmegreen & Falgarone 1996), the measured fractal dimension of interstellar gas (Kritsuk et al. 2007a; Federrath, Klessen & Schmidt 2009, and references therein) and the few per cent efficiency with which gas is converted into stars (Padoan 1995; Vázquez-Semadeni, Ballesteros-Paredes & Klessen 2003; Krumholz & McKee 2005; Elmegreen 2008), and most likely determines in large part the mass distribution of star forming cores [the core mass distribution (CMD); Ballesteros-Paredes et al. 2006; Dib et al. 2008] and possibly the mass distribution of stars

⋆E-mail: daniel.price@sci.monash.edu.au

© 2010 The Authors. Journal compilation © 2010 RAS

themselves, i.e. the initial mass function (IMF; Padoan, Nordlund & Jones 1997; Padoan & Nordlund 2002; Hennebelle & Chabrier 2008). However, given that a full theory of turbulence is elusive even in the incompressible regime apart from the phenomenology provided by Kolmogorov (1941), one inevitably turns to numerical simulations to glean insight.

Given the importance of numerical simulations in understanding the basic statistics of supersonic turbulence, and the possible implications for star formation theory, it is crucial that results inferred from such simulations are robust with respect to different numerical methods and codes. This has motivated at least two major code comparison projects in the last year or so in which both of the present authors have been involved. The 'Potsdam comparison' (Kitsionas et al. 2009) compared simulations of decaying, hydrodynamic turbulence using seven different codes [three smoothed particle hydrodynamics (SPH) codes and four grid-based codes] at a fixed resolution (215^3 particles for the SPH codes and 256^3 grid cells for the grid codes). The results showed generally good agreement on statistics such as the density probability distribution functions (PDFs) and power spectra, similar to earlier studies (Mac Low et al. 1998; Klessen, Heitsch & Mac Low 2000). In a similar spirit, the KITP07 comparison[1] compared a large number of grid-based and SPH calculations of decaying turbulence, for both hydrodynamics and magnetohydrodynamics (MHD), at a range of resolutions, though the results are yet to be published.

Both of these comparisons are problematic in several respects. The first is that it is difficult to make a statistical comparison using decaying turbulence, since the time evolution is limited and therefore only a few instantaneous snapshots can be compared. Instantaneous snapshots, however, are subject to intermittent fluctuations that make a head-to-head comparison based on single time slices difficult (Kritsuk et al. 2007a; Federrath et al. 2010). Secondly, both comparisons start from evolved initial conditions, produced from either a previously driven SPH simulation (Potsdam) or a grid-based calculation (KITP) that has to be interpolated and/or downsampled to/from the grid/particles appropriate to the different codes, with an ensuing loss of accuracy and consistency before the comparison has even begun (this problem is much worse for the MHD case where differences in divergence-free representations for the magnetic field between codes is a further issue).

In this paper, we consider only two codes: an SPH code, PHANTOM, and a grid-based code, FLASH, which we take to be broadly representative of the fundamentally different classes of code used for star formation studies (the codes are described in Section 2). The turbulence in both codes is driven from stationary, uniform initial conditions with exactly the same energy input and driving pattern over multiple turbulent crossing times. We also consider a range of resolutions (128^3, 256^3 and 512^3 in both grid elements and the number of SPH particles) in order to estimate resolution requirements and establish where convergence has occurred in one code or the other, or neither. In the present work we limit ourselves to a study of hydrodynamic turbulence, that is, without magnetic fields. This is primarily because the algorithms for MHD in SPH that are currently being used for star formation studies (e.g. Price & Bate 2008) rely on formulating the magnetic field in terms of Euler potentials, an approach which cannot be used for turbulence studies over multiple crossing times due to the restricted field representations (see Price 2010 for recent progress).

The goals of this paper are to (i) establish whether or not agreement can be found between SPH and grid codes on the basic statistics of supersonic turbulence, (ii) define resolution criteria for various statistical measures of supersonic turbulence such as power spectra, PDFs and structure functions and (iii) establish the relative strengths and weaknesses of each method for turbulence studies. We discuss the numerical methods in Section 2, with the Fourier space driving discussed in Section 2.2. Results from both codes are presented in Section 3 and our findings discussed in Section 4.

2 NUMERICAL METHOD

2.1 Equations

We solve the equations of non-self-gravitating hydrodynamics given by

$$\frac{\partial \rho}{\partial t} + (\boldsymbol{v}\cdot\nabla)\rho = -\rho\nabla\cdot\boldsymbol{v}, \tag{1}$$

$$\frac{\partial \boldsymbol{v}}{\partial t} + (\boldsymbol{v}\cdot\nabla)\boldsymbol{v} = -\frac{\nabla P}{\rho} + \boldsymbol{f}_{\rm stir}, \tag{2}$$

where $\boldsymbol{f}_{\rm stir}$ is a stirring force, the details of which are discussed in Section 2.2. The pressure is related directly to the density via an isothermal equation of state

$$P = c_{\rm s}^2\rho, \tag{3}$$

where, since the equations are scale-free to all but the Mach number, we use $c_{\rm s} = 1$. We solve (1)–(3) using periodic boundary conditions in the three-dimensional domain $x, y, z \in [0, 1]$. The initial conditions are a uniform density medium $\rho = \rho_0 = 1$ with zero initial velocities.

We discuss our results in terms of the dynamical time, defined as $t_{\rm d} \equiv L/(2\mathcal{M})$, where L is the box size and $\mathcal{M}$ is the rms Mach number. However, the absence of a physical scale in the equations means that the results can be arbitrarily scaled to the interstellar medium by defining length-, mass- and time-scales. For example, adopting a length-scale of 10 pc and a sound speed of 0.2 km s^{-1} gives the physical time from $t/t_{\rm d}$ according to

$$t_{\rm physical} = 2.5\ {\rm Myr}\left(\frac{L}{10\ {\rm pc}}\right)\left(\frac{c_{\rm s}}{0.2\ {\rm km\,s^{-1}}}\right)^{-1}\frac{t}{t_{\rm d}}. \tag{4}$$

One can similarly set a mass-scale by defining the initial density to be $n_0 \approx 3\times10^2$ cm^{-3}, i.e. $\rho_0 \approx 10^{-21}$ g cm^{-3} assuming fully molecular hydrogen gas, giving a total mass in the box of $\sim 1.5\times10^4$ M$_\odot$. For these parameters, the maximum density reached in our calculations from turbulent fluctuations alone is $\rho_{\rm max} \sim 10^{-17}$–$10^{-16}$ g cm^{-3} or $n_{\rm max} \sim 10^6$ cm^{-3} (see Fig. 2) for the highest resolution SPH calculation.

2.2 Driving

For driving turbulence, we use the same driving routine used in Schmidt, Hillebrandt & Niemeyer (2006), Federrath, Klessen & Schmidt (2008), Federrath et al. (2009, 2010) and Schmidt et al. (2009). The driving routine updates a vector of real values according to an algorithm that generates an Ornstein–Uhlenbeck or 'coloured noise' sequence (e.g. Eswaran & Pope 1988). The sequence x_n

[1]Initiated at a star formation workshop held during 2007 at the Kavli Institute for Theoretical Physics (KITP) in Santa Barbara: http://kitpstarformation07.wikispaces.com/Star+Formation+Test+Problems

is a Markov process that takes the previous value, weights by an exponential damping factor with a given autocorrelation time t_s and drives by adding a Gaussian random variable, weighted by a second damping factor, also with correlation time t_s. For a time-step dt, this sequence can be written as

$$x_{n+1} = f x_n + \sigma \sqrt{(1 - f^2)}\, z_n, \tag{5}$$

where $f = \exp(-\mathrm{d}t/t_s)$, z_n is a Gaussian random variable drawn from a Gaussian distribution with unit variance and σ is the desired variance of the Ornstein–Uhlenbeck sequence (see e.g. Bartosch 2001). The resulting sequence satisfies the properties of zero mean and stationary rms equal to σ. Its power spectrum in the time domain can vary from white noise [$P(f) =$ constant] to 'brown' noise [$P(f) \propto 1/f^2$].

The physical force field is constructed in the Fourier space using the Ornstein–Uhlenbeck process. This allows a simple decomposition of the field into a solenoidal (divergence-free) part and a compressible (curl-free) part using a Helmholtz decomposition. In this study, we only keep the solenoidal part. Inverse Fourier transformation yields the physical solenoidal force field $\boldsymbol{f}_{\rm stir}$ used in equation (2). A more detailed description of the forcing module applied here is provided in Federrath et al. (2010).

The time-dependent Fourier modes for constructing the forcing patterns $\boldsymbol{f}_{\rm stir}$ were calculated and written to a file before the actual numerical experiments. Both the SPH and the grid codes read exactly the same forcing sequence from this file. Thus, it was guaranteed that both codes were using exactly the same forcing at all times during the comparison experiments.

2.3 FLASH (grid)

2.3.1 Hydrodynamics

FLASH (Fryxell et al. 2000; Dubey et al. 2008) is an adaptive-mesh refinement code (Berger & Colella 1989) that uses the piecewise parabolic method (PPM; Colella & Woodward 1984) to solve the equations of hydrodynamics. The PPM provides a shock capturing scheme to keep shocks and contact discontinuities sharp (typically spreading over two to three zones), while maintaining third-order accuracy in smooth flows through a parabolic reconstruction scheme. In this study, FLASH v3 was used, which provides a uniform grid mode. Thus, the overhead in storing and iterating the adaptive-mesh hierarchy was completely removed, which yields a speed-up of factors of a few. FLASH is parallelized using the message passing interface (MPI). For the resolutions studied here (128^3, 256^3 and 512^3 grid cells), one, eight and 64 MPI processes, respectively, were used in a mode of parallel computation, each calculation taking roughly 12, 250 and 5000 CPU hours, respectively. FLASH has been extensively tested against laboratory experiments (Calder et al. 2002) and other codes (Dimonte et al. 2004; Heitmann et al. 2005; Kitsionas et al. 2009).

2.3.2 Tracer particles

FLASH provides an option for Lagrangian tracer particles, which can be evolved alongside the hydrodynamics. Similar to SPH particles, tracer particles provide information in the Lagrangian frame, but unlike SPH particles, the tracer particles have no feedback on the hydrodynamics, i.e. the variables on the grid are independent of the tracers. The tracer particles' x, y and z positions can be any real number within the computational domain, not bound to the grid. However, they are moved with the velocity computed on the grid. The velocity is interpolated at the exact position of each tracer particle for each time-step using a first-order cloud-in-cell interpolation scheme. Higher order interpolation schemes such as the triangular-shaped-cloud scheme can also be used instead. However, we used the first-order scheme here, because various tests suggested no strong dependence of our results on the interpolation scheme. The tracer particles were moved on the hydrodynamic time-step with the grid-interpolated velocity using a first-order scheme. We initialized 128^3, 256^3 and 512^3 tracer particles at $t = 0$ on a uniform grid at exactly the same positions as the SPH particles were initialized in the PHANTOM calculations (see Section 2.4.4), matching the grid and SPH resolutions (128^3, 256^3 and 512^3, respectively). Adding the tracer particles does not add any significant computational overhead to the FLASH calculations, apart from the additional memory requirements.

In order to extract the maximum possible information from the tracer particles, we have computed – in post-processing – a density field based solely on the tracer particle positions. This is achieved by assuming that they are particles of fixed mass (dividing the total mass in the simulation by the number of tracer particles) and using the SPH density calculation routine from PHANTOM where the density and smoothing length are iterated self-consistently (based on equations 6 and 7). Column-integrated and cross-section slice plots of the density field were then produced as for the PHANTOM results using SPLASH (Price 2007).

2.4 PHANTOM (SPH)

PHANTOM is a low-memory, highly efficient SPH code written especially for studying non-self-gravitating problems. The code is made very efficient by using a simple neighbour-finding scheme based on a fixed grid and linked lists of particles. The calculations shown in this paper have used only the shared memory OPENMP parallelization in PHANTOM, using four, eight and 32 processors and requiring 265, 5050 and 120 000 CPU hours for the 128^3, 256^3 and 512^3 calculations, respectively. Thus, the 256^3 PHANTOM calculation was roughly comparable in computational cost to the 512^3 FLASH calculation and similarly for the 128^3 PHANTOM versus 256^3 FLASH (though some caution is required here due to the different machines and architectures used to run each code). One may also consider that PHANTOM was found to be roughly an order of magnitude faster than 'standard' SPH codes in the Kitsionas et al. (2009) turbulence comparison.

2.4.1 Hydrodynamics

For hydrodynamics PHANTOM implements the full variable smoothing length SPH formulation developed by Price & Monaghan (2004) and Price & Monaghan (2007), whereby the smoothing length, h, and density, ρ, are mutually dependent via the density sum (for particle a)

$$\rho_a = \sum_b m_b W_{ab}(h_a), \tag{6}$$

which is an exact solution to (1), and the relation

$$h_a = \eta \left(\frac{m_a}{\rho_a}\right)^{1/3}, \tag{7}$$

where m is the particle mass and $W_{ab} \equiv W(|\boldsymbol{r}_a - \boldsymbol{r}_b|, h_a)$ is the SPH smoothing kernel (see e.g. Monaghan 1992; Price 2004; Monaghan 2005 for reviews of SPH). Equations (6) and (7) are iterated self-consistently using a Newton–Raphson method as described in Price & Monaghan (2007), where in this paper we have used $\eta = 1.2$,

giving approximately 58 neighbours per particle in a smooth distribution.

The fact that the smoothing length has a functional dependence on (ultimately) the particle position means that the derivatives of h can be accounted for in the equations of motion, resulting in exact conservation of momentum, angular momentum, energy and entropy in the SPH equations. In PHANTOM, the equations of motion (2) take the form

$$\frac{\mathrm{d}\boldsymbol{v}_a}{\mathrm{d}t} = -\sum_b m_b \left[\frac{P_a + q_a}{\Omega_a \rho_a^2} \nabla_a W_{ab}(h_a) + \frac{P_b + q_b}{\Omega_b \rho_b^2} \nabla_a W_{ab}(h_b) \right] + \boldsymbol{f}_{\rm stir}, \quad (8)$$

where P is the pressure, Ω is a dimensionless quantity related to the smoothing length gradients (see Price & Monaghan 2007 for details) and q represents the artificial viscosity term (discussed below). In the absence of shock dissipation ($q = 0$), there is zero numerical dissipation contained in the above equations and energy is conserved to the accuracy of the time-stepping scheme – here a Kick-Drift-Kick leapfrog integrator equivalent to the velocity Verlet method, implemented with individual particle time-steps. For an isothermal equation of state, the viscosity term q therefore represents the only numerical form of energy loss.

2.4.2 Artificial viscosity

Shocks are treated in PHANTOM using a standard artificial viscosity term, though formulated slightly differently to the usual SPH expression in order to obtain a more efficient calculation. Instead of the usual expression we write the artificial viscosity as q in (8), where

$$q_a = \begin{cases} \frac{1}{2}\alpha_a \rho_a v_{{\rm sig},a} |\boldsymbol{v}_{ab} \cdot \hat{\boldsymbol{r}}_{ab}|, & \boldsymbol{v}_{ab} \cdot \hat{\boldsymbol{r}}_{ab} < 0 \\ 0 & \boldsymbol{v}_{ab} \cdot \hat{\boldsymbol{r}}_{ab} \geq 0 \end{cases}, \quad (9)$$

where $\boldsymbol{v}_{ab} \equiv \boldsymbol{v}_a - \boldsymbol{v}_b$ and we use

$$v_{{\rm sig},a} = c_{\rm s,a} + \beta_{\rm visc} |\boldsymbol{v}_{ab} \cdot \hat{\boldsymbol{r}}_{ab}| \quad (10)$$

as the maximum signal velocity for hydrodynamics. The β term in the signal velocity provides a non-linear term that was originally introduced to prevent particle penetration in high Mach number shocks (see e.g. Monaghan 1989). Indeed, one of our findings from this comparison is that sufficient β-viscosity is an important factor for accurate SPH calculations in the supersonic regime. We use $\beta_{\rm visc} = 4$ in this paper, the motivation for which is discussed further in Section 3.2.1 and demonstrated in Appendix A.

The artificial viscosity described above is essentially the same as the Monaghan (1997) formulation with a slightly different averaging of the density and signal velocity. We use the Morris & Monaghan (1997) switch to reduce dissipation away from shocks, in which the dissipation parameter α is evolved according to a source and decay equation

$$\frac{\mathrm{d}\alpha_a}{\mathrm{d}t} = -\frac{\alpha_a - \alpha_{\rm min}}{\tau_a} + \mathcal{S}_a, \qquad \tau_a = h_a/(\sigma c_{\rm s}), \quad (11)$$

where we have used $\sigma = 0.1$, $\mathcal{S} = \max(0, -\nabla \cdot \boldsymbol{v})$, $\alpha_{\rm min} = 0.05$, enforced $\alpha_{\rm max} = 1.0$ and given all particles $\alpha = \alpha_{\rm min}$ initially.

2.4.3 Boundary conditions

Periodic boundary conditions are implemented in PHANTOM by directly finding neighbours across the periodic boundary and interacting with a distance in each direction calculated according to

$$(x_a - x_b) = \min\left[(x_a - x_b), (|x_a - x_b| - L)\frac{x_a - x_b}{|x_a - x_b|} \right], \quad (12)$$

where L is the box size in the corresponding direction. This gives a significant memory saving since memory does not have to be assigned to the storage of ghost particles.

2.4.4 Initial conditions

The SPH particles were set up initially on a regular cubic lattice, using equal mass particles, identical to the set-up used for the Lagrangian tracer particles in the FLASH calculations (Section 2.3.2).

3 RESULTS

Both codes have been run using the same driving pattern for 10 dynamical times ($t = 0.5$ in code units) and at a resolution of 128^3, 256^3 and 512^3 elements. For the grid code, this resolution is fixed spatially throughout the evolution, giving fixed resolution in volume but variable resolution in mass, whilst for the SPH code the particles move following the fluid motion, giving equal resolution in mass but variable resolution in volume. The two methods are therefore very nicely complementary for assessing the statistics of supersonic turbulence for different quantities which may be either mass- or volume-weighted. It should be noted that whilst grid-based calculations of ISM turbulence have been run at much higher resolutions – up to 2048^3 (see Kritsuk et al. 2007a) with resolutions of 1024^3 even in early simulations of decaying turbulence (Porter, Woodward & Pouquet 1998) – our use of 134 217 728 SPH particles (512^3) represents the highest resolution turbulence simulation performed to date with an SPH code, over an order of magnitude higher than the 'high-resolution' calculation (10 million particles) in Ballesteros-Paredes et al. (2006) and two-and-a-half orders of magnitude higher than the $\sim$200 000 particles used for many of the runs in that paper and elsewhere (Klessen et al. 2000; Vázquez-Semadeni et al. 2003).

3.1 Time evolution of global variables

The time variations of the mass-weighted rms Mach number and of the maximum gas density are shown in Figs 1 and 2, computed at every time-step for both codes. The mass-weighted rms Mach number in SPH is simply the square root of the average value of $v^2/c_{\rm s}^2$ on the particles, whilst in FLASH this has been computed using the rms value of $\rho v^2/(\rho_0 c_{\rm s}^2)$, to correspond to the SPH average.

The Mach number evolution (Fig. 1) is similar in both codes and at all resolutions of up to around $4t_{\rm d}$, at which point all calculations show variations of the order of 5 per cent from each other. No clear trends either between codes or with resolution are apparent, indicating that the variation observed is due to the stochastic nature of fully developed turbulence producing different though statistically similar evolution (see Fig. 3 for the evidence for this in the density field). It is these intermittent fluctuations that make turbulence code comparisons based on snapshot-to-snapshot comparison difficult, because the instantaneous turbulence field will quickly diverge between different codes in the fully developed regime because of the chaotic nature of the turbulence (see projections and slices for $t \gtrsim 2t_{\rm d}$ comparing the SPH and grid results).

The evolution of maximum density (Fig. 2) shows strong time variability in all six calculations, similar to the results shown in

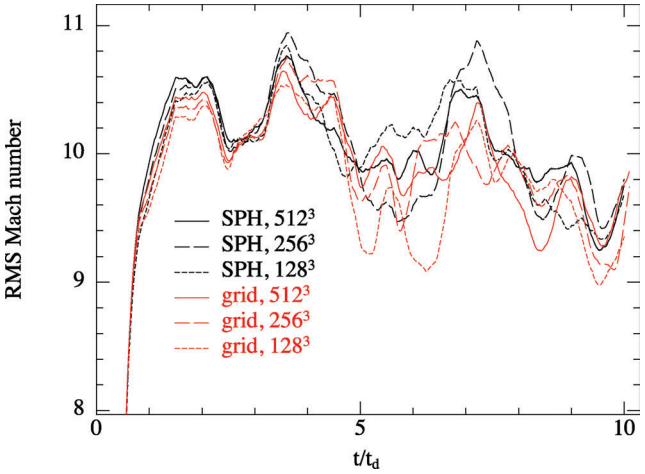

Figure 1. Mass-weighted rms Mach number as a function of time for the six calculations, as indicated in the legend. The time evolution is similar for both the SPH and the grid codes and for all resolutions up to $\sim 4t_{\rm d}$, where all calculations show deviations from each other of the order of 5 per cent in $\delta\mathcal{M}/\mathcal{M}$ though with no systematic trends with either code or resolution.

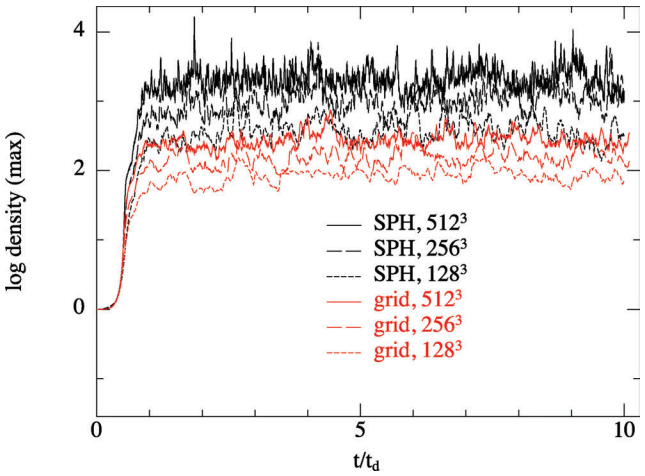

Figure 2. Maximum density as a function of time in the calculations using PHANTOM (SPH) and FLASH (grid) at resolutions of 128^3, 256^3 and 512^3 particles/grid cells, as indicated in the legend. The evolution shows strong time variability, a consequence of the intermittency inherent in the lognormal probability distribution function (increasingly higher densities have correspondingly smaller probabilities). The maximum density is therefore also a strong function of resolution in each code. At 128^3 particles, the SPH code resolves maximum densities similar to those achieved at 512^3 on the grid.

Kritsuk et al. (2007a, fig. 2) and Federrath et al. (2009, fig. 2). For isothermal flows arbitrarily large density fluctuations can be produced, though with vanishingly small probability as can be inferred from the lognormal form of the PDF. This simply reflects the highly intermittent nature of the density fluctuations in supersonic, turbulent flows. The maximum density is a clear function of resolution in each code, showing no signs of convergence, as one might expect seeing as we are sampling the very highest data point in the PDF. The results also demonstrate the evidently higher mass resolution in the SPH code: at 128^3 particles, the maximum density resolvable in SPH is roughly similar to that resolved at 512^3 on the grid. Using 512^3 SPH particles, the maximum density resolved at rms Mach 10 is roughly three-and-a-half orders of magnitude above the mean density which one might therefore expect to be similar to the mass resolution in a 2048^3 grid-based calculation.

3.2 Density field

3.2.1 Projected density fields

The projected column density fields at the highest resolution (512^3) are shown for PHANTOM, FLASH and the density field computed from the FLASH tracer particles in Fig. 3 (left-hand, middle and right-hand panels, respectively), at intervals of $\Delta t = 1t_{\rm d}$ for the first four dynamical times. The column density plots for SPH have been produced directly from the particles to a 2D pixel map using the SPLASH visualization tool (Price 2007) whilst the grid-based results have been integrated through the grid. We show the integration through the z-direction in the codes.

At early times, the calculations show clear agreement in the location of individual shocks ($t = 1t_{\rm d}$, first row) and in the development of large-scale structures ($t = 2t_{\rm d}$, second row). By $t = 4t_{\rm d}$ (fourth row) there is no longer clear correspondence even at the largest scales between codes, in agreement with the observed deviations in the time evolution of the rms Mach number around this time (Fig. 1).

In terms of resolution, high-density structures appear better resolved in the SPH calculations at the same number of computational elements. However, the grid results tend to show better resolution of features in low density regions, as one might expect since in SPH the resolution is preferentially shifted *away* from low density regions towards high density regions.

The excellent agreement between codes in the development of individual shock structures within the first dynamical times (first row) enabled us to make a very detailed comparison of features between codes which proved to be very helpful in the comparison process. In particular it highlighted that, with the parameters we were initially using, some of the dense structures created by the collision of one or more shocks were rapidly losing definition in the SPH results, resulting in a noisy density field that was rather unlike the grid results (this is shown in more detail in Appendix A). The problem could be easily traced to be caused by particles penetrating or 'overshooting' the shock front in these high Mach number shocks, a problem which the non-linear β (von Neumann–Richtmyer) term in the SPH artificial viscosity (equations 9–10) was designed to prevent (see Monaghan 1989). The problem was thus easily fixed by using a larger value for $\beta_{\rm visc}$. We have therefore used $\beta_{\rm visc} = 4$ throughout the paper, rather than the nominal $\beta_{\rm visc} = 2$ which is widely used – and sufficient – for low Mach number calculations. It should be noted that this makes very little difference to the overall dissipation rate since the linear viscosity term (α) dominates the numerical dissipation rate almost everywhere except at very strong divergence in the velocity field (where particle penetration can occur).

Comparing the projected column density fields calculated using the tracer particles in the FLASH calculation (right-hand panels) to the grid-based density field (middle panels), showing a wealth of sub-grid structures, suggests that the tracer particles have the ability to provide a truly staggering improvement in resolution in the density field. The improved resolution is all the more remarkable considering that the tracer particles are merely advected with the grid-based velocity field at essentially no extra computational expense.

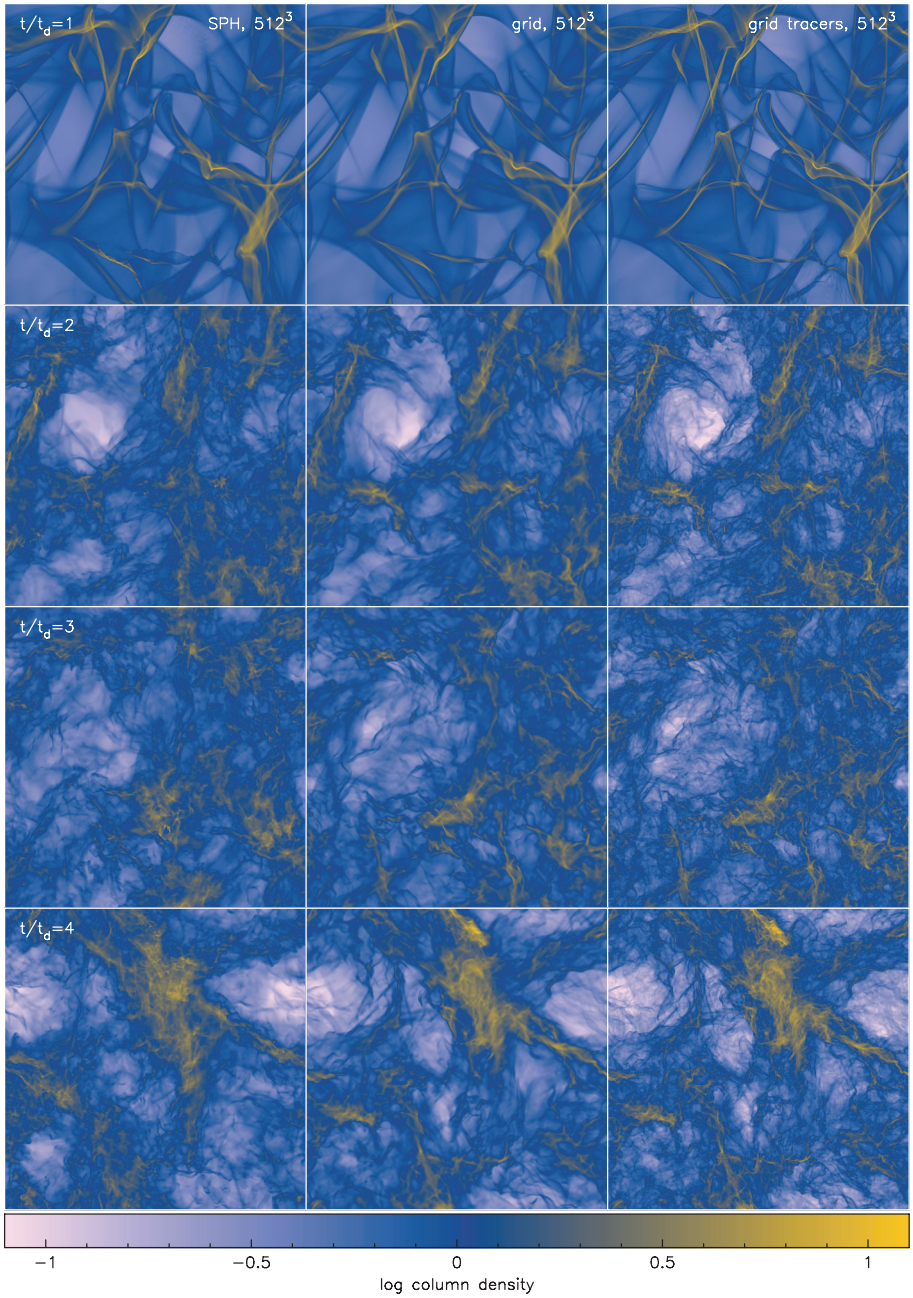

Figure 3. Projected column density in the PHANTOM (SPH, left-hand panels) and FLASH (grid, middle panels) calculations at a resolution of 512^3 particles/grid cells, showing the evolution over the first few dynamical times (top to bottom), together with the density computed from the tracer particle positions in the FLASH calculation using an SPH density estimate (right-hand panels). After 1 dynamical time (first row), there is clear correspondence in individual shock structures between the SPH and the grid code, whilst after 2 dynamical times (second row) there are similar large-scale features. However by 3 or 4 dynamical times (third and fourth rows) only a weak correlation even between large-scale features is observed. Dense features are in general better resolved in the SPH calculations at equivalent resolutions (in a number of particles = number of grid cells sense), whilst the grid-based calculations tend to better resolve features in low density regions (see also Fig. 5). The increased resolution of sharp features in the tracer particle density fields (right-hand panels, compared to middle panels) suggests a remarkable ability for the tracer particles to provide information on sub-grid scales at essentially zero additional computational cost.

3.2.2 Cross-section slices

Column density plots such as those shown in Fig. 3 in general tend to highlight dense features, since all structures along the line of sight contribute to the projected field (which also tends to be the case in observations). The features in column density plots are therefore reflected by statistics such as the PDF (Figs 6–8) and quantities such as the maximum density (Fig. 2). However volumetric quantities such as the volume filling factor of the material and the velocity field, reflected in statistics such as power spectra and structure functions, are better illustrated by cross-section slices. For this reason we show cross-section slices of density at the mid-plane of the computational domain ($z = 0.5$), showing a resolution study of the initial shock development at 1 dynamical time (Fig. 4) and a comparison of the evolved snapshots at the end of the simulations ($t/t_{\rm d} = 10$), showing only the highest resolution (Fig. 5). The plots show the density field

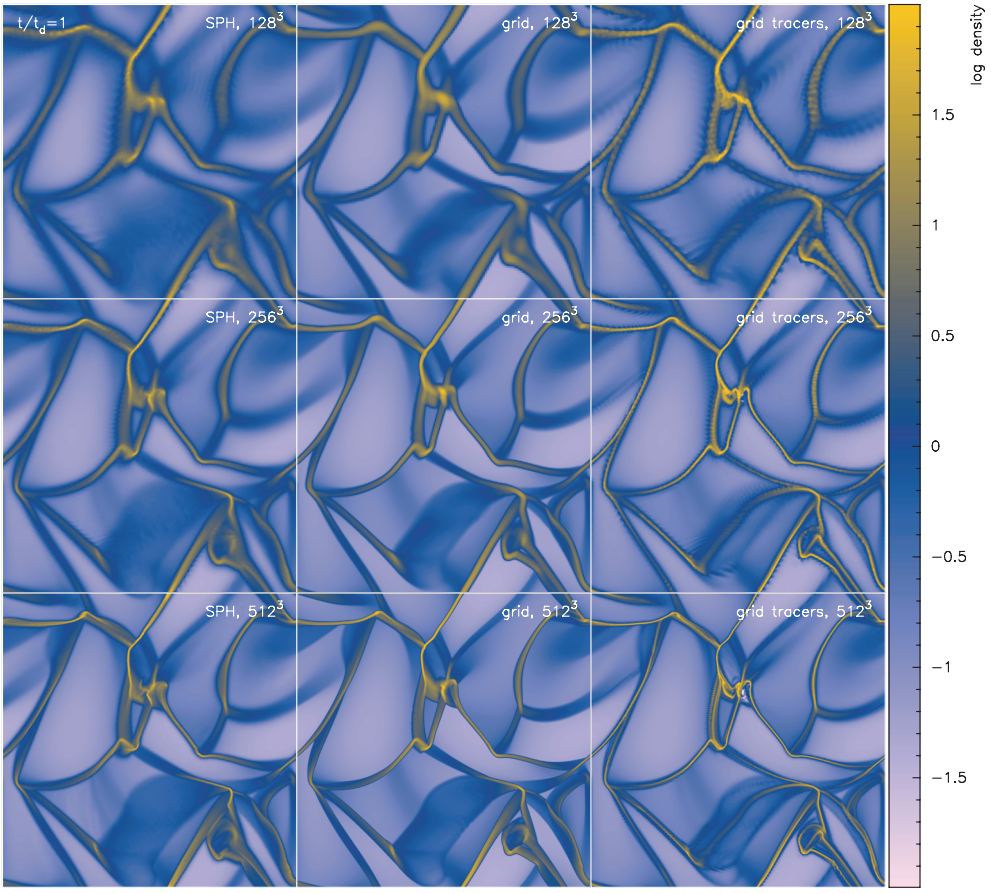

Figure 4. Cross-section slice of the density at the box mid-plane ($z = 0.5$) after 1 dynamical time, for three different resolutions (128^3, 256^3 and 512^3 in grid cells/particles, top to bottom) using PHANTOM (SPH, left-hand panels), FLASH (grid, middle panels) and for the density calculated from the tracer particles in the grid calculation using an SPH summation (right-hand panels).

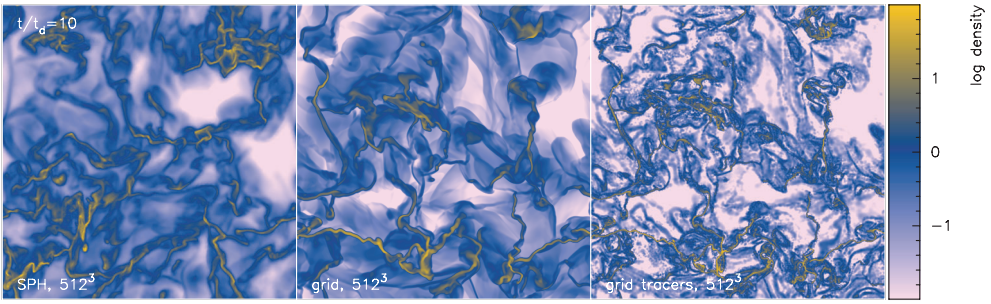

Figure 5. Cross-section slice of the density at the box mid-plane ($z = 0.5$), as in Fig. 4 but here shown after 10 dynamical times and showing only the highest resolution calculations (512^3). The FLASH calculations (grid, middle panel) shows better resolution in low density regions compared to PHANTOM (SPH, left-hand panel). In evolved snapshots, the tracer particles appear strongly clustered in high density regions and almost completely absent from the voids (right-hand panel).

using PHANTOM (left-hand panels in Figs 4 and 5), FLASH (middle panels in Figs 4 and 5) and for the tracer particle density field computed from the FLASH calculations (right-hand panels).

Figs 4 and 5 show clearly that the grid results are better resolved in low density regions. The resolution in the SPH calculations is concentrated towards high density regions which fill relatively little of the volume. Comparing individual shock structures in Fig. 4 shows that in general the shocks have better definition in FLASH, with the shock widths in the highest resolution PHANTOM calculation similar to those obtained at 256^3 in FLASH. This is as might be expected given the relative crudeness of the shock capturing scheme (artificial viscosity) in the SPH code compared to the PPM shock capturing scheme (Colella & Woodward 1984) employed in FLASH. In the more evolved snapshots (Fig. 5), the grid results show many well-defined shock features in low density regions that are much less well resolved in the SPH calculations.

Some numerical artefacts are visible in the lowest resolution SPH calculations in the earliest snapshot ($t = 1t_{\rm d}$, top-left panel of Fig. 4) due to the 'breaking' of the initial regular lattice on which the particles were placed as it is distorted by the flow. Interestingly, similar artefacts are visible – and more accentuated – in the low-resolution tracer particle plots (top-right panel). These effects are

not obviously visible either in the SPH or in the tracer particles at higher resolution (middle and bottom rows of Fig. 4) or at later times (Fig. 5) once the particles have adopted a more 'natural' arrangement. There are no obvious artefacts at low resolution in the grid-based calculation.

Density slices calculated from the tracer particles in the FLASH calculation are shown in the rightmost panels of Figs 4 and 5, using the SPH density summation (6) iterated self-consistently with the smoothing length according to (7). Comparison with the grid-based density field at 1 dynamical time, the tracer particles appear to substantially increase the resolution in high density regions. Whilst most of the features have close correspondence to those visible in the grid slices (middle panels of Fig. 4), it is notable that a dense shock structure appears in the lower part of the $t/t_{\rm d} = 1$ snapshots at all resolutions that is completely absent from both the SPH and grid density fields. The absence of this feature even at 512^3 in the middle panels of Fig. 4, yet clearly present at 128^3 in the tracer particles, suggests that it may be an artefact of tracer particles clustering below the grid scale. At later times (right-hand panel of Fig. 5), this is even more evident by the fact that the tracer particles are strongly concentrated in high density regions and largely evacuated from low density regions (i.e. large parts of the panels are saturated at the density floor of the plot due to the absence of a contribution from tracer particles even with iterated smoothing lengths).

The difference between the density slices and column density plots shows that in general, *for similar numbers of computational elements* (not the same as equal computational expense), SPH codes are better at resolving dense structures (highlighted by projections through the volume), whilst grid codes are better at resolving volumetric structures (highlighted by slices though the volume).

3.3 Probability distribution functions

Many studies have demonstrated that the density probability distribution function (PDF) in supersonic turbulence is well represented by a lognormal distribution (e.g. Padoan et al. 1997; Passot & Vázquez-Semadeni 1998; Klessen 2000; Kritsuk et al. 2007a; Federrath et al. 2008; Lemaster & Stone 2008; Federrath et al. 2010), i.e.

$$p(\ln\rho)\mathrm{d}\ln\rho = \frac{1}{\sqrt{2\pi\sigma^2}}\exp\left[-\frac{1}{2}\left(\frac{\ln\rho - \overline{\ln\rho}}{\sigma}\right)^2\right]\mathrm{d}\ln\rho, \quad (13)$$

where the mean of the logarithm of density $\ln\rho$ is related to the standard deviation σ of $\ln\rho$ by

$$\overline{\ln\rho} = -\sigma^2/2. \quad (14)$$

The appearance of a lognormal form in isothermal flows can be understood analytically as a consequence of the multiplicative central limit theorem assuming that individual density perturbations are independent and random (Vazquez-Semadeni 1994; Passot & Vázquez-Semadeni 1998; Nordlund & Padoan 1999). In physical terms, this means that density fluctuations at a given location are constructed by successive passages of shocks with a jump amplitude independent of the local density (Ballesteros-Paredes et al. 2007; Kritsuk et al. 2007a; Federrath et al. 2010). Furthermore, the width of the PDF for $\ln\rho$ is found to be related to the rms Mach number according to

$$\sigma^2 = \ln(1 + b^2\mathcal{M}^2), \quad (15)$$

where the factor $b \approx 1/2$ has been suggested by early numerical experiments (e.g. Padoan et al. 1997). More recently, Kritsuk et al. (2007a) found a much lower value of $b \approx 0.26$ whilst Beetz et al. (2008) found $b = 0.37$. Brunt (2010) has also recently measured $b = 0.5$ in the Taurus Molecular Cloud, based on a method for inferring the 3D variance from 2D observations developed by Brunt, Federrath & Price (2010). Federrath et al. (2008, 2010) reconcile these results by showing that the width of the PDF depends not only on the rms Mach number but also on the relative degree of compressible and solenoidal modes in the forcing, with $b = 0.33$ appropriate for purely solenoidal forcing and $b = 1$ for purely compressive forcing. Lemaster & Stone (2008) – performing calculations at a range of Mach numbers – suggest that relationship (15) should be adjusted, finding $\sigma^2 = -0.72\ln(1 + 0.5\mathcal{M}^2) + 0.20$ from a three-parameter fit for hydrodynamic turbulence. For the purposes of the comparison at hand, we simply fit the PDFs using a single parameter b based on equations (13)–(15).

3.3.1 *Volume-weighted PDFs*

Time-averaged PDFs of $s \equiv \ln(\rho/\rho_0)$ for the three SPH calculations and three grid calculations are shown in Figs 6–8. The plots show the time average of individual PDFs computed at intervals of $\Delta t = t_{\rm d}/10$, starting from $2t_{\rm d}$ when turbulence is reasonably well established (see Figs 1 and 3). This gives a total of 81 snapshots used in the averaging procedure. For reference, we compute the PDF for each code with a bin width of 0.1 in $\ln\rho$, with the first bin starting at $(\ln\rho)_{\rm min} = -12$.

For the grid results, the volume-weighted PDF is constructed simply by binning the grid cells according to the value of $\ln\rho$. To obtain a volume-weighted PDF in SPH, it is necessary to weight the contribution of each particle by the volume element associated with that particle, m/ρ, which for equal mass particles is simply inversely proportional to the density. To construct the PDF we therefore bin each particle according to the value of $\ln\rho$ and add a contribution of $1/\rho$ to the bin, normalizing the resultant PDF such that the integral

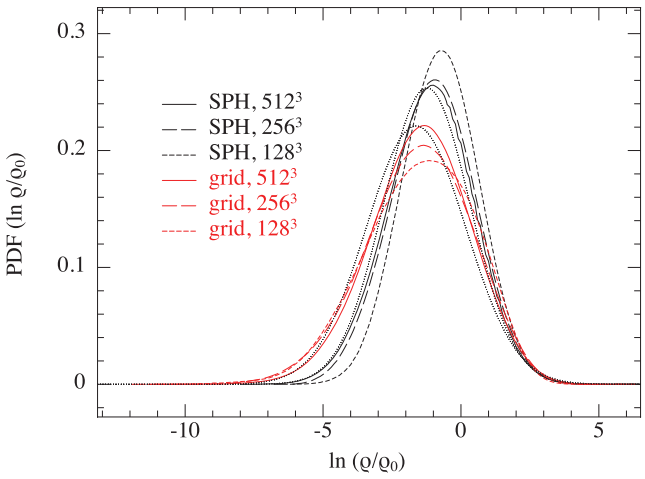

Figure 6. Time-averaged PDF of the logarithm of the density field $s \equiv \ln\rho$ from the PHANTOM [SPH, dark (black in online version) lines other than dotted] and FLASH [grid, lighter (red in online version) lines] calculations, each at resolutions of 128^3, 256^3 and 512^3 particles/grid cells. The PDFs are averaged over 81 snapshots evenly spaced between $t/t_{\rm d} = 2$ and $t/t_{\rm d} = 10$. Here we show the PDFs on a linear scale to highlight the change in the position of the peak value as a function of resolution. We have also plotted, as dotted black lines, the best-fitting (to the peak) lognormal distributions from equations (13) and (15) using $b = 0.5$ (best fitting the 512^3 grid results) and $b = 0.33$ (best fitting the 512^3 SPH results). The SPH and grid results show complementary trends with resolution.

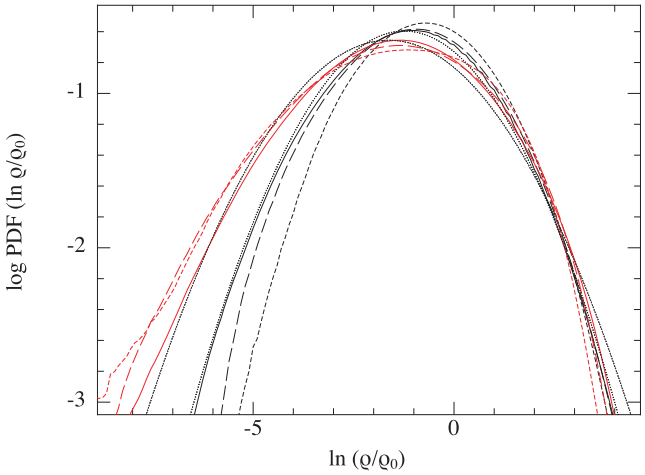

Figure 7. PDF of $\ln \rho$, as in Fig. 6, but here shown on a logarithmic scale. The PDFs are lognormal to good approximation for ∼3−4 orders of magnitude in density either side of the mean, demonstrated by the best-fitting lognormal distributions (fitted to the peak in Fig. 6) given by the dotted black lines using $b = 0.5$ and $b = 0.33$ to fit the 512^3 grid [lighter (red) solid line] and 512^3 SPH [darker (black) solid line] results, respectively.

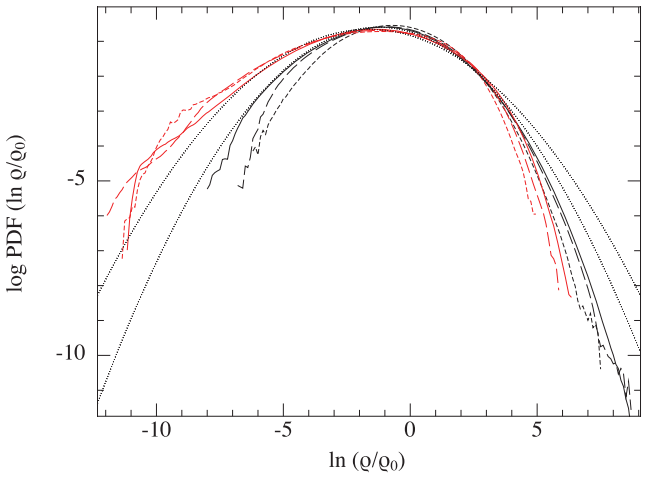

Figure 8. Time-averaged PDFs, as in Figs 6 and 7 but here showing the tails of the distributions at very low and very high densities. The SPH code [dark (black) lines other than dotted] resolves the PDF to much higher densities than the grid code [lighter (red) lines], though the grid results correspondingly extend further into the low density regime. The lognormal distributions (dotted black lines) are no longer a good approximation to the distribution very far from the mean, in particular in the high density tail (where the 256^3 and 512^3 SPH results appear to show convergence).

over all bins (i.e. the total probability) is unity. This is different to the procedure used to construct density PDFs from SPH particles used both in the Potsdam comparison (Kitsionas et al. 2009; see, however, fig. 11 in Kitsionas et al. 2009)) and by previous authors (e.g. Mac Low et al. 1998; Klessen 2000; Vázquez-Semadeni et al. 2003), whereby the SPH results were first interpolated to a grid and a PDF constructed as above for the grid-based results. The main disadvantage to interpolating to the grid is that the part of the high density tail of the SPH calculation that falls below the grid scale is removed. To retain this tail requires that PDFs *should not* be constructed from SPH particles by interpolating to a grid, though this is a perfectly valid procedure for computing volumetric quantities such as power spectra (see Section 3.4).

The PDFs thus constructed (Fig. 7) show clearly a lognormal distribution in agreement with many previous calculations and with theoretical expectations (see above). Whilst the results are broadly similar for all calculations in the central regions around the mean density and in overall shape, clear differences may also be observed between codes and with resolution, particularly in the tails of the distribution (Fig. 8). At the low density end (Fig. 8), the grid results tend to show a wide, low density tail, with probability densities *decreasing* with resolution. By contrast, the SPH results show a narrower low density tail with probability densities that *increase* with resolution.

Whilst both codes appear to be converging towards each other, it is clear that neither is well converged at the low density end ($\rho/\rho_0 \lesssim 0.01$) at least for the resolutions used in this paper. Thus, the low density tail should not be used to fit the PDF width from either grid or SPH codes alone at these resolutions. Instead, we measure the PDF width using the best fit around the mean value (i.e. based on Fig. 6). The resulting best-fitting lognormal distributions are plotted as dashed lines in Fig. 6, corresponding to $b = 0.33$ for the 512^3 SPH results and $b = 0.5$ for the 512^3 grid results. As it turns out, the best-fitting lognormal distributions also provide a good fit to the low density tails (Figs 7 and 8), though the same is not true at very high density (see Fig. 8).

At the high density end, the trend with resolution for both codes is for the PDF in the high density tail to increase slightly, increasing the PDF width. The FLASH results show a stronger trend with resolution at high densities and appear to converge towards the PHANTOM results, with rough equivalence between the 512^3 grid-based results and the 128^3 SPH results in resolving the high density tail, similar to what is observed for the evolution of maximum density in Fig. 2. Interestingly, the SPH results appear converged between the 256^3 and 512^3 calculations for densities up to around $\rho/\rho_0 \sim 10^3$ (though not to the best-fitting lognormal; see below), with the primary effect of the additional resolution at 512^3 being to extend the tail to lower probabilities (but with similar overall width).

The facts that the SPH results appear close to converged between the 256^3 and 512^3 and that the grid results are converging towards them suggest that a value of $b \approx 0.35$–0.4 would be the converged value. This is similar to the results of Beetz et al. (2008) for solenoidal forcing ($b = 0.37$) and close to the prediction of $b = 1/3$ for solenoidal forcing from the heuristic model for the b parameter presented in Federrath et al. (2008, 2010).

The reason for the discrepancy at high density merits some consideration given the importance of this regime in relation to star formation. The most straightforward conclusion is that the convergence we find is merely incidental and that performing calculations at higher resolution would resolve the remaining discrepancy. Certainly, resolution requirements on the PDF become greater at higher Mach numbers because of the stronger time variability in the tails of the distribution. This is evident from the strong fluctuations in $\rho_{\max}$ (Fig. 2) that are up to an order of magnitude larger than the fluctuations shown in fig. 2 of Kritsuk et al. (2007a). There may also be differences due to the random forcing algorithm. In particular Federrath et al. (2010), using the same (solenoidal) forcing algorithm employed here, also find a small deviation from lognormality at the high density end, though smaller than we find since they employ 1024^3 elements and a lower Mach number (Mach 6). They also found strong deviations from lognormality when a compressible forcing was applied, indicating that the PDF at high densities is quite sensitive to the forcing employed. Federrath et al. (2010) discuss intermittency as a cause of non-Gaussian PDF tails. They quantify and discuss the Mach-number–density correlations as the

key to non-Gaussian PDFs (see Vazquez-Semadeni 1994; Passot & Vázquez-Semadeni 1998). Falgarone et al. (1994) and Hily-Blant, Falgarone & Pety (2008) also find strong intermittent fluctuations in their molecular cloud observations and attribute them to a fundamental property of turbulence, i.e. intermittency (see e.g. She & Leveque 1994).

In principle, it is also possible to compute the PDFs from the tracer particle density field calculated with the SPH summation. However, we find that the resulting PDFs show a strong deviation from a lognormal distribution, particularly in the high density tail (much stronger than those seen in Fig. 8 and in the opposite direction), due to the manner in which tracer particles tend to cluster in high density regions at later times (see the discussion in Section 3.2.2 and right-hand panels in Fig. 5).

3.4 Power spectra

Padoan & Nordlund (2002) derive a relationship between the mass distribution of dense cores to the slope of the kinetic energy power spectrum in supersonic, super-Alfvénic turbulence via the relation

$$N(m)\mathrm{d}\log m \propto m^{-3/(4-\beta)}\mathrm{d}\log m, \tag{16}$$

where β is the slope of the kinetic energy power spectrum assumed to be a power law of the form

$$E(k) \propto k^{-\beta}, \tag{17}$$

where β would be $\sim 5/3$ according to the Kolmogorov (1941) phenomenology for incompressible turbulence. Supersonic turbulence is generally found to have a power spectrum closer to the completely pressure-free shock-dominated turbulence produced by solving Burgers' equation, $\beta = 2$, implying dominance of the non-linear advection term $(v\cdot\nabla)v$ over the pressure gradient in the equation of motion. A value consistent with the observed Salpeter (1955) slope for the IMF of $N(m)\mathrm{d}\log m \propto m^{-4/3}\mathrm{d}\log m$ requires $\beta \approx 1.75$, which Padoan & Nordlund (2002) suggest arises from supersonic MHD turbulence in the super-Alfvénic regime.

Recently, Kritsuk et al. (2007a) have suggested that Kolmogorov scaling may be applicable for highly compressible turbulence by assuming that the mean volume energy transfer rate $\rho v^2 v/l$ is constant, implying that $E(k) \propto k^{-5/3}$ holds for the variable $w \equiv (\rho^{1/3}\boldsymbol{v})$ rather than simply for the velocity. We thus consider the power spectra of both quantities.

We have computed the power spectra for each code directly from gridded data using the same analysis script for both codes. For the SPH code, this means that the results have first been interpolated to grids of size 256^3, 512^3 and 512^3 cells for the 128^3, 256^3, 512^3 particle calculations, respectively. The interpolation has been performed using a routine from the SPLASH visualization code, the details of which are described in Price (2007). The main disadvantage of interpolating SPH data to a grid is that any resolution in the SPH code on scales smaller than the grid scale is lost. This is most obvious when comparing quantities such as the maximum density on the particle data compared to the maximum density on the interpolated grid. For example, the maximum density interpolated on to a 512^3 grid [$\max(\rho/\rho_0) \sim 3$–4×10^2] is a factor of ~3–4 lower than the maximum density from the particles [$\max(\rho/\rho_0) \sim 1$–2×10^3] for snapshots from the 512^3 SPH calculation, which would remove some of the information from the high density tail of the PDF as discussed above. Whether or not the interpolation procedure affects the power spectrum calculation can be determined simply by comparing the results from interpolations to different sized grids. We find that for the power spectrum, as one might expect given that it is a volumetric measurement, the power spectra are identical for different grid sizes apart from ks very close to the grid scale.

Power spectra

$$E(\boldsymbol{k}) = \frac{1}{2}\tilde{\boldsymbol{w}}(\boldsymbol{k})^2 \tag{18}$$

for an arbitrary vector field $\boldsymbol{w}$ are constructed from the 3D Fourier transform,

$$\tilde{\boldsymbol{w}}(\boldsymbol{k}) = \frac{1}{(2\pi)^3}\int_V \boldsymbol{w}(\boldsymbol{x})\mathrm{e}^{-\mathrm{i}2\pi\boldsymbol{k}\cdot\boldsymbol{x}}\mathrm{d}^3\boldsymbol{x}, \tag{19}$$

The angle-averaged power spectrum was then obtained by the standard procedure of summing $E(\boldsymbol{k})$ in bins according to the norm of the wavenumber $|k|$ (as in e.g. Kitsionas et al. 2009).

3.4.1 *Volume-weighted velocity power spectra*

The velocity power spectrum (that is, where $\boldsymbol{w} \equiv \boldsymbol{v}$), averaged over 81 snapshots as described above for the PDFs, is shown – compensated by k^2 – in Fig. 9 for the three SPH calculations (solid black lines) and for the three grid calculations (dashed red lines). The results, similar to previous studies, show a peak at the driving scale $k \sim 2$, a power-law slope (flat in these compensated spectra) between $k \sim 4$ and up to $k \sim 12$ in the highest resolution calculations, and an extended dissipative tail at large k. Both codes show a power-law slope close to the pressure-free Burgers model slope of k^{-2}. The trend with resolution is for both codes to tend towards a slightly shallower slope, with the highest resolution calculations consistent with $\sim k^{-1.95} - k^{-1.98}$ for both codes at 512^3, depending on whether or not the results for $7 < k < 12$ are interpreted as an inertial range or as a bottleneck effect. The extent of the power-law scaling range of the velocity power spectrum appears to be very similar in both codes at equivalent (number of grid cells = number of particles) resolutions, though the SPH results show a faster drop-off towards higher k in the dissipative tail in agreement with the results by Kitsionas et al. (2009).

These results are entirely consistent with the power-law slopes obtained in fig. 2 of Padoan et al. (2007). However, they differ

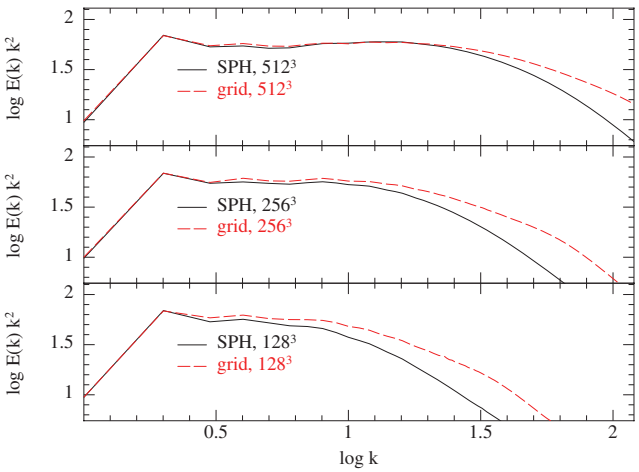

Figure 9. Velocity power spectra ($\frac{1}{2}v^2$), shown compensated by k^2 as an average over 81 snapshots evenly spaced between $t/t_\mathrm{d} = 2$ and $t/t_\mathrm{d} = 10$ for the SPH (solid, black) and grid (dashed, red) calculations at the three different resolutions, as indicated. For calculations at or above 256^3 computational elements in either code the results in the scaling range $7 \lesssim k \lesssim 11$ are consistent with a slope slightly shallower than Burgers' value of k^{-2}, between $k^{-1.93}$ and $k^{-1.98}$ depending on whether or not the $7 \lesssim k \lesssim 11$ region is interpreted as an inertial range or a bottleneck effect.

strongly from the low-resolution SPH and grid results shown in fig. 2 of Ballesteros-Paredes et al. (2006), shown compensated in fig. 8 of Padoan et al. (2007). In particular, our SPH results show power-law slopes consistent with $\beta = 2$ or *shallower*, which is in stark contrast to the $\beta = 2.7$–2.9 obtained by Ballesteros-Paredes et al. (2006), albeit at lower Mach numbers (6 and 3, respectively). This can be understood primarily as an effect of the numerical resolution, since we observe a significantly steeper slope in our low-resolution SPH calculations shown in Fig. 9. As noted in Section 1, however, the resolution in our 'low' resolution SPH calculation, employing 2.1 million particles, is already an order of magnitude higher than the ∼200 000 particles used for most of the calculations in Ballesteros-Paredes et al. (2006) (they perform one 'high' resolution calculation using ≈10 million particles, the power spectrum of which is not shown in their paper, though it is used to derive a CMD). We also find excellent agreement between the SPH and grid-based results which is in contrast to Ballesteros-Paredes et al. (2006) where the measured slopes differ between their codes which had been attributed to the very different properties of the SPH and Total Variation Diminishing schemes used in their paper.

3.4.2 *Density-weighted velocity power spectra ($\rho^{1/3}\boldsymbol{v}$)*

Fig. 10 shows the time-averaged power spectrum, computed as above, of the quantity $\boldsymbol{w} \equiv \rho^{1/3}\boldsymbol{v}$, which according to the hypothesis of Kritsuk et al. (2007a) is the quantity that for supersonic turbulence should show a Kolmogorov-like scaling of $k^{-5/3}$. We have therefore compensated the spectra by $k^{5/3}$ in order to assess whether or not this can be supported on the basis of our calculations. The spectra in Fig. 10 show similar generic features to those observed in Fig. 9.

The lower resolution calculations (128^3 and 256^3) in both codes show slopes that appear shallower than $\beta = 5/3$, though the convergence of both codes is towards a steeper slope with resolution. In particular the 512^3 calculations with both codes show a small, flat region in the compensated spectrum between $k \sim 4$ and $k \sim 6$ that may be interpreted as a resolved inertial range (shown by the dotted black line) consistent with the Kritsuk et al. (2007a) scaling, with a 'bottleneck effect' for $k > 6$ extending into the dissipative tail. For the grid code, this is consistent with the findings of Kritsuk et al. (2007a) and Federrath et al. (2010) that 512^3 is roughly the minimum resolution required to resolve the inertial range, and we conclude that a similar requirement holds for SPH.

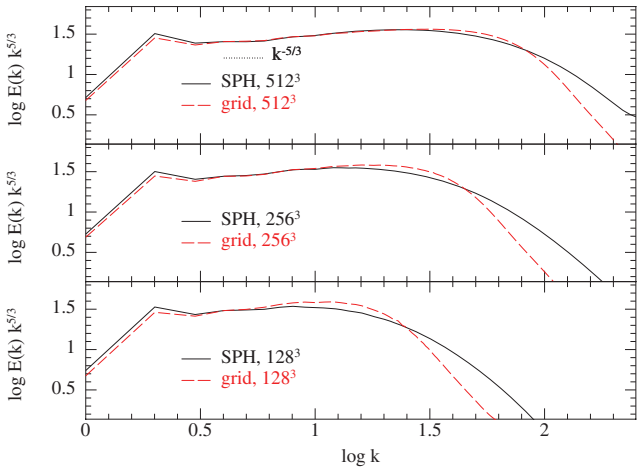

Figure 10. Density-weighted velocity power spectra, as in Fig. 9 but for the quantity ($\rho^{1/3}\boldsymbol{v}$) instead of the velocity field. There is tentative evidence of a flat portion in the compensated spectra at resolutions above 256^3 in either code, suggesting a small scaling range in the region of $4 \lesssim k \lesssim 6$ (dotted line) consistent with a Kolmogorov-like $k^{-5/3}$ scaling for this quantity as suggested by Kritsuk et al. (2007a). This also suggests that 512^3 particles/grid cells is the minimum resolution requirement to determine the power spectrum slope in the inertial range in either code (see also Federrath et al. 2010, fig. C.1).

Interestingly, the difference between codes in the rate of drop-off in the high-k dissipative tail for the $\rho^{1/3}\boldsymbol{v}$ spectrum is the reverse of what occurs for the velocity field alone (comparing to Fig. 9). That is, for $\rho^{1/3}\boldsymbol{v}$ the grid-based results drop off much faster at high-k than the SPH code, whereas the SPH code drops off faster in the velocity spectrum. We interpret this as being due to the fact that SPH has better *mass* resolution for equal numbers of computational elements (reflected in the density field) but worse *volume* resolution (reflected in the velocity field). This is further evident in the spectrum of the density field alone, discussed below.

3.4.3 *Density power spectra*

Fig. 11 shows the power spectra of the density field, computed as the spectrum of density fluctuations $\delta\rho \equiv \rho - \bar{\rho}$ such that the integral under the power spectrum gives the density variance. Whilst not well fitted by a single power law, we show the spectra compensated by k^2 to facilitate the comparison. The overall shape of the spectra is similar between codes on large scales (small k), though it is clear that the SPH code shows a much higher resolution in the density field, falling much more slowly at high k compared to the grid results at comparable resolutions and explaining the results in Fig. 10 as intermediate between Figs 9 and 11. The SPH density spectrum at 128^3 particles appears better resolved than the 256^3 grid spectrum though not as well resolved as the 512^3 grid spectrum, lying somewhere between the two.

3.5 Structure functions

We have measured the structure functions

$$S_p(l) \equiv \langle |\boldsymbol{w}(\boldsymbol{r} + \boldsymbol{l}) - \boldsymbol{w}(\boldsymbol{r})|^p \rangle \quad (20)$$

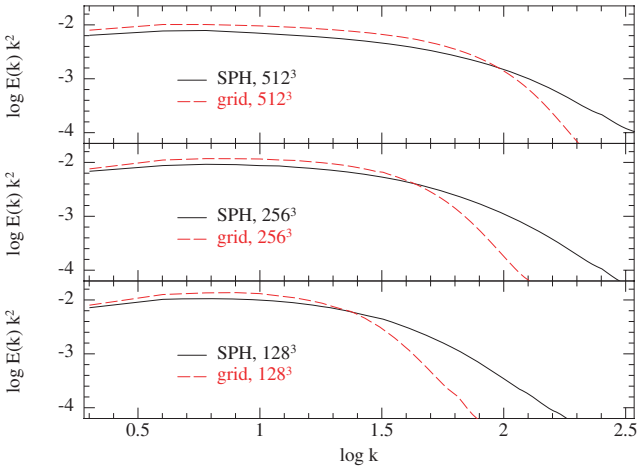

Figure 11. Power spectra, as in Figs 9 and 10, but here for the density field, computed as the spectrum of the density fluctuations $\delta\rho \equiv \rho - \bar{\rho}$. Clearly, the SPH code provides increased resolution in the density field at high k compared to the grid-based code for the same number of computational elements. The spectra have been compensated by k^2, though it is evident that the slope of the density spectrum is not well described by a single power law.

© 2010 The Authors. Journal compilation © 2010 RAS, MNRAS **406,** 1659–1674

from our calculations, where in this paper we show orders up to 5, i.e. $p = 1, 2, 3, 4$ and 5 and the variable $\boldsymbol{w}$ is either the velocity $\boldsymbol{w} \equiv \boldsymbol{v}$ or the quantity $\boldsymbol{w} \equiv (\rho^{1/3}\boldsymbol{v})$ as for the computation of the power spectra in the previous section. We compute intrinsically three-dimensional structure functions (rather than the approximate 'directionally split' versions used e.g. in the KITP comparison) by sampling pairs of either grid cells or SPH particles, computing the relative velocity difference and adding the result (the absolute value to the power p) to the appropriate bin corresponding to the spatial separation of the points (the 'lag' – given here in computational units, i.e. in terms of the box length L). Dividing by the total number of contributions to each bin produces the average, as indicated by the angle brackets $\langle \cdots \rangle$. We have computed the structure functions for both the transverse ($\boldsymbol{w}$ perpendicular to the line $\boldsymbol{l}$ joining the pair of points) and longitudinal ($\boldsymbol{w}$ parallel to $\boldsymbol{l}$) components of $\boldsymbol{w}$ in each case.

Calculation of the structure functions is computationally expensive, in principle requiring a summation over $\mathcal{O}(N^2)$ pairs of points. A more efficient calculation can be made by selecting only a subsample of points. We achieve this by randomly selecting a fixed number of points (either grid cells or particles) and computing the pairwise interaction of these sample points with all points in the computational domain, with a constraint to achieve similar sampling of all lags. For the structure function calculations, we typically use ∼250 000 sample points. For the SPH results we have first computed structure functions by interpolating the SPH data to a grid, as described above for the power spectra. Whilst this ensures that the analysis step is identical to the grid-based results, this procedure has the disadvantage that the SPH densities and velocities are smoothed by the interpolation step. For comparison, we have therefore computed structure functions also directly from the particle data. In the particle version, we iterate the structure functions to completion by progressively increasing the number of sample points by a factor of 2 and check that the error between the final result and the structure functions using half the number of sample points is small (typically, we require the rms error on the highest order structure function to be <1 per cent). In practice, this produces a similar sample size to that used for the grids, i.e. a few hundred thousand sample points for a 512^3 calculation, but can be more efficient if the velocity field is well ordered (e.g. at early times).

3.5.1 *Velocity structure functions*

The structure functions for the velocity field ($\boldsymbol{w} \equiv \boldsymbol{v}$) at all computed orders ($p = 1, \ldots, 5$) are shown in the left-hand panel of Fig. 12 for the 512^3 calculations with both codes. The structure functions show the same general features in both codes, showing slopes that appear power-law-like in the range from $l \sim 0.03$ to 0.3 (though see below), a flat structure around the driving range ($0.3 \lesssim l \lesssim 0.5$) and a fall-off in the dissipative tail ($l \lesssim 0.03$). The transverse

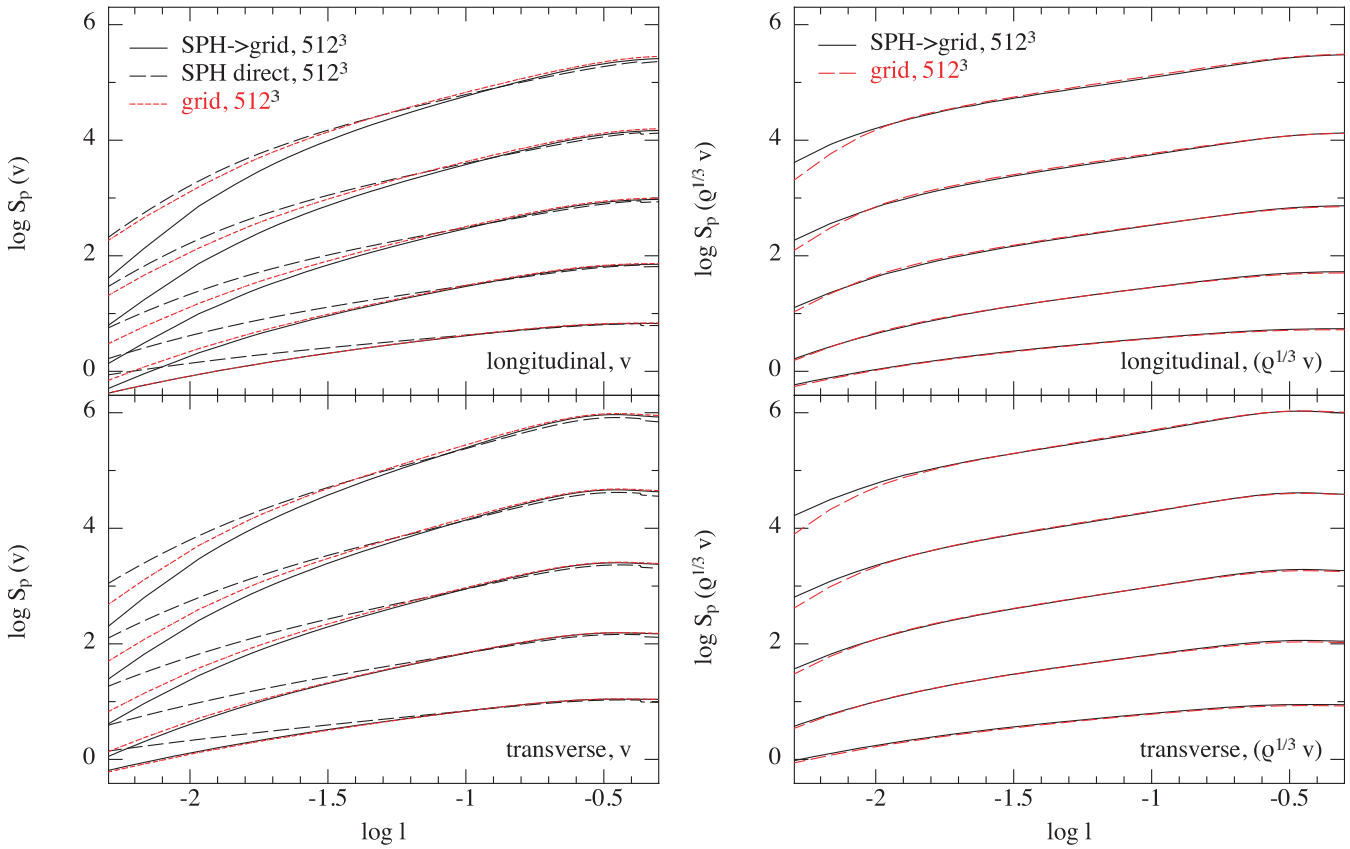

Figure 12. Structure functions $S_p \equiv \langle |\boldsymbol{w}(\boldsymbol{r}+l) - \boldsymbol{w}(\boldsymbol{r})|^p \rangle$ as a function of spatial separation (the lag, l), for orders $p = 1$, 2, 3, 4 and 5, showing the time average over 81 snapshots evenly spaced from $t_\mathrm{d} = 2$ to $t_\mathrm{d} = 10$ in each case. Structure functions are shown for the longitudinal ($\boldsymbol{w} \| \boldsymbol{l}$, top) and transverse ($\boldsymbol{w} \perp \boldsymbol{l}$, bottom) components of the velocity field, $\boldsymbol{w} \equiv \boldsymbol{v}$ (left), and for the mass-weighted velocity, $\boldsymbol{w} \equiv \rho^{1/3}\boldsymbol{v}$ (right). The results from the FLASH (grid) 512^3 calculation are given by the dashed red lines whilst the PHANTOM (SPH) results at 512^3 are shown by the solid black lines, where these have first been interpolated to a 512^3 grid in order to be analysed identically to the grid results. Results for the velocity field computed directly from the SPH particles for the 512^3 calculation are plotted in the left-hand panels using dashed black lines.

structure functions appear flatter around the driving scale compared to the longitudinal version, consistent with the fact that we have used purely solenoidal forcing. Differences between codes mainly appear in the dissipative tail, as observed also in the power spectra (Figs 9 and 10). In the velocity structure functions, as with the velocity power spectrum, it appears that the SPH results fall off faster in the dissipative tail (comparing solid and dot–dashed lines in the left-hand panel of Fig. 12), though the results computed directly from the particles (dashed lines) appear to show a slower fall-off, indicating that at least some of this may be an artefact of the interpolation procedure. However, the structure functions computed directly from the particles also show much shallower slopes at the lowest orders ($p = 1, \ldots, 4$), so it is not clear that the structure functions computed in this manner are truly comparable.

3.5.2 *Density-weighted velocity structure functions ($\rho^{1/3}\boldsymbol{v}$)*

Following Kritsuk et al. (2007b), we have also computed structure functions for $\boldsymbol{w} \equiv (\rho^{1/3}\boldsymbol{v})$. These are shown in the right-hand panels of Fig. 12, showing – given the above – only the versions computed identically from a grid (i.e. interpolated in the SPH case). Again, the qualitative features are in good agreement between the two codes – in particular, the structure functions for $\rho^{1/3}\boldsymbol{v}$ show a power-law scaling range over a much wider range of distances, $0.01 \lesssim l \lesssim 0.3$. As was the case for the power spectra (see Fig. 10), with the density-weighting the grid code (solid lines) shows a faster fall-off in the dissipative tail compared to the SPH code (dashed lines), in contrast to the pure velocity version (comparing the right-hand and left-hand panels in Fig. 12).

3.6 Structure function scaling

A more quantitative analysis can be made by performing a least-squares fit to determine the structure function slope ζ_p assuming $S_p \propto l^{\zeta_p}$ for each order p. The results of such a fit to the time-averaged structure functions shown in Fig. 12 – performed over a fixed Δl in the range $0.1 < l < 0.15$ (see below) – are shown in Fig. 13. Plotted are the fitted slope ζ_p at each order as a function of p, for both the velocity structure functions (left-hand panel) and the density-weighted versions (right-hand panel). The results from the SPH code, computed from the grid-interpolated structure functions, are shown in black, whilst the FLASH (grid) results are shown in red. In order to quantify the time variability in the value of the slope, we have also computed the standard deviation in the structure function slope at each order computed for each of the 81 snapshots discussed above. The 1σ deviations are plotted as the error bars in Fig. 13.

For the velocity structure functions (left-hand panel of Fig. 13), reasonable agreement between codes is seemingly obtained for the two lowest order structure functions ($p = 1$ and 2) at the highest resolution employed (512^3, though see below). The grid code (dashed red lines) appears close to (though not fully) self-converged at these orders (but not for $p > 2$), whilst the SPH code (solid black lines) appears only close to convergence at the lowest order. The situation appears slightly better for the $\rho^{1/3}$-weighted structure functions (right-hand panel of Fig. 13), where the grid code (dashed red lines) shows apparent convergence in the slopes up to $p = 3$ between the 256^3 and 512^3 calculations. The SPH results (solid black lines) appear to show only a small change between the measured slopes at all orders between the 256^3 and 512^3 results, though given the remaining disagreement between codes even at 512^3 it is not clear that true convergence has been reached in either.

The somewhat large caveat to the results shown in Fig. 13 is our finding that the determined slope depends strongly on the range of scales ($\Delta l \equiv l_{\rm max} - l_{\rm min}$) used to perform the least-squares fit. This is discussed in more detail in Appendix B and demonstrated by Fig. B1 that shows the dependence of ζ_p on the employed Δl for the transverse structure functions. It is clear from the fact that the measured slope steepens as Δl is increased that relatively little true power-law scaling range is apparent in either code at the resolutions employed. This is particularly true for the velocity structure functions (left-hand panel of Fig. B1) where either a very short ($\Delta l \lesssim 0.02$) scaling range exists or none at all. The situation is marginally improved for the density-weighted structure functions (right-hand panel of Fig. B1), where the measured slope is less dependent on the fitting range (also apparent from Fig. 13). However, there remains a significant dependence on Δl even for the lowest order $p = 1$. Furthermore, it is clear that any nominal convergence between 256^3 and 512^3 results in individual codes seen

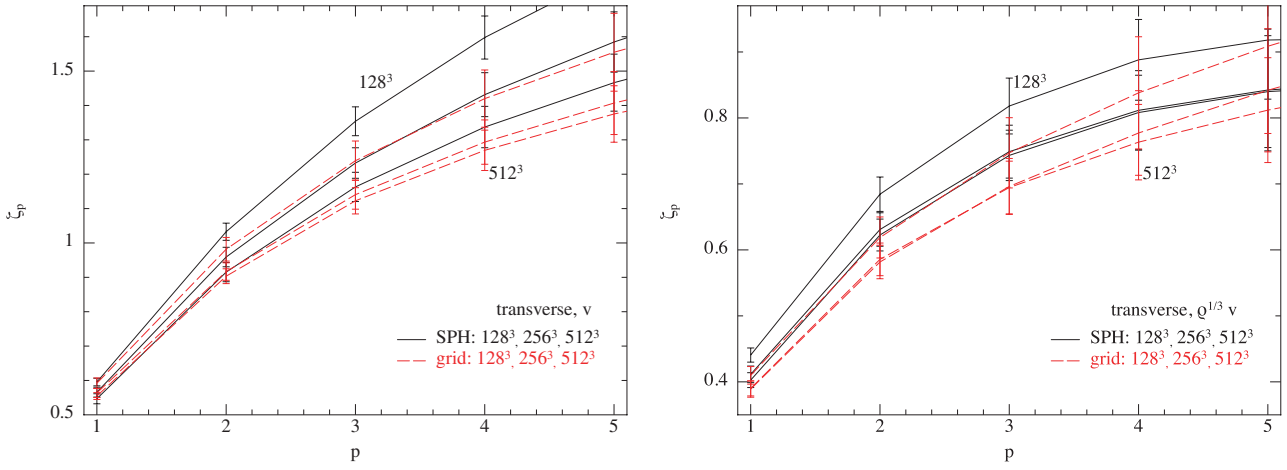

Figure 13. Time-average of the measured structure function slope ζ_p, where $S_p \propto l^{\zeta_p}$ for the transverse velocity (left-hand panel) and $\rho^{1/3}\boldsymbol{v}$ (right-hand panel), averaged from 81 snapshots evenly spaced between $t/t_{\rm d} = 2$ and $t/t_{\rm d} = 10$ and plotted as a function of the structure function of the order of p. The solid black lines correspond to the PHANTOM (SPH) calculations whilst the dashed red lines correspond to the FLASH (grid) calculations, each shown at three different resolutions (the slopes decrease with resolution in both codes). Error bars show the 1σ errors in the time average of the measured slope. The corresponding time average of the structure functions themselves are shown in the bottom panels of Fig. 12.

© 2010 The Authors. Journal compilation © 2010 RAS, MNRAS **406,** 1659–1674

in Fig. 13 *only* occurs if a relatively short range in l ($\Delta l \lesssim 0.05$, i.e. $0.1 \lesssim l < 0.15$) is used to perform the fit (and, as noted above, the measured slopes in this range also do not agree between codes). It is therefore difficult to assert that either code produces a resolved scaling in either the velocity- or density-weighted structure functions at *any order* at these resolutions.

Given the above, we have not attempted a detailed comparison with phenomenological models for the structure function scaling, such as those proposed by She & Leveque (1994) [revised for supersonic turbulence by Boldyrev (2002); Schmidt, Federrath & Klessen (2008)]. Nevertheless, although the true structure function scaling remains to be determined, it is clear that the scaling for both v and $\rho^{1/3}v$ does not match either the Kolmogorov (1941) ($\zeta_p \propto p/3$) or Burgers ($\zeta_p = 1$ for $p > 1$) expectations and also does not match the Boldyrev (2002) theory, though the relative scaling we have measured does compare reasonably well to the parameters suggested by Schmidt et al. (2008).

4 DISCUSSION AND CONCLUSIONS

In this paper, we have performed a detailed comparison of the statistics of supersonic turbulence using high-resolution numerical simulations with two fundamentally different codes: FLASH, a Eulerian grid-based code, and PHANTOM, a Lagrangian particle-based SPH code. Despite the very different numerical methods we find in general very good agreement between the codes on the many aspects of supersonic turbulence, though it is clear that neither code shows results that are fully converged at 512^3 except for a small scaling range in the velocity power spectrum with both codes and some indication of convergence near the peak and at the high density end of the PDF in the SPH case.

We find good agreement in the fact that hydrodynamic turbulence at Mach 10 has a velocity power spectrum with a slope around $E(k) \propto k^{-1.95}$, very close to Burger's value of $E(k) \propto k^{-2}$, confirming many previous results using only grid-based codes (e.g. Padoan et al. 2007; Federrath et al. 2010). At the highest resolution employed, both codes support the idea that the power spectrum of the mixed quantity $\rho^{1/3}\boldsymbol{v}$ shows a Kolmogorov-like scaling in the power spectrum of $k^{5/3}$, as proposed by Kritsuk et al. (2007a). Both codes agree that the PDF of the logarithm of the density shows a distribution that is lognormal to good approximation for densities of around three to four orders of magnitude either side of the mean density, with the factor b relating the width to the Mach number measured to lie between $b = 0.33$ and $b = 0.5$, with the converged value expected to lie somewhere around $b \approx 0.4$. However, both codes also show that there are significant deviations from a lognormal distribution at high density, as also found by Federrath et al. (2010).

Our conclusions regarding resolution and computational requirements are as follows.

(i) For measuring volumetric statistics such as the power spectrum slope and structure function scaling, we find that SPH and grid codes give roughly comparable results when the number of SPH particles is approximately equal to the number of grid cells. This means that SPH codes are not well suited to measuring such quantities since for this kind of problem, an SPH code will be significantly more expensive than a uniform-grid implementation at similar numbers of computational elements [we find the cost of the SPH calculations with PHANTOM similar to the cost of running the grid code (FLASH) at twice the resolution, i.e. with 256^3 particles $\approx 512^3$ grid cells in terms of CPU time].

(ii) On the other hand, the SPH code was found to be better at resolving dense structures, giving maximum densities at a resolution of 128^3 particles that were similar to the maximum densities resolved in the grid code at 512^3 cells, reflected also in the high density tail of the PDF. SPH is therefore a more efficient method in this regard, which is an important reason why it is frequently used for studying star formation (for which a grid-based code requires adaptive-mesh refinement, adding a significant computational overhead).

(iii) At comparable resolutions ($N_{\rm part} \approx N_{\rm cells}$), SPH (PHANTOM) appears to be more dissipative (steeper dissipative tails in the power spectrum and structure functions) in the velocity field, but the reverse is true for the statistics of the density-weighted quantity $\rho^{1/3}\boldsymbol{v}$ where the grid (FLASH) results appear more dissipative. We attribute the former to the greater sophistication of the shock capturing scheme in the grid-based code and the latter to the better resolved power in the density field provided by the SPH code.

(iv) The absolute values of the structure function slopes are not converged in either grid or SPH at 512^3, requiring much higher resolution in order to make a meaningful comparison with scaling models.

(v) In order to accurately simulate supersonic turbulence in SPH, it is important to ensure that sufficient β-viscosity is applied to prevent particle interpenetration in shocks. At Mach 10, we require $\beta_{\rm visc} = 4$ instead of the usual $\beta_{\rm visc} = 2$.

(vi) We find that calculation of the sub-grid density field from the tracer particle distribution using an SPH summation can significantly enhance the resolution of high density structures from the grid-based results. However, it is unclear whether or not the statistics of these sub-grid structures can be used in a meaningful way, because of the manner in which tracer particles tend to cluster in high density regions.

The above conclusions mean that the differences between the SPH and grid-based results discussed by Padoan et al. (2007), at least in terms of the power spectrum slope, can be understood as a consequence of the low resolution employed in the SPH calculations rather than being due to an intrinsic difficulty with the method. Given this, it is also likely that the conclusions drawn by Ballesteros-Paredes et al. (2006) regarding the presence or otherwise of an emergent power-law slope in the CMD should also be treated with caution. As a follow-up to this paper, it would be interesting to examine the properties of dense clumps (or 'cores') in our calculations using a clump-finding algorithm in a similar manner to Ballesteros-Paredes et al. (2006) and Padoan et al. (2007) to see whether or not these differences can also be reconciled by improved resolution in the SPH results.

ACKNOWLEDGMENTS

We thank the anonymous referee for comments that have substantially improved the paper and Aake Nordlund for kind provision of some of the analysis routines used to make a preliminary comparison. This work was initiated whilst CF was visiting Monash University under the Go8/DAAD Joint Research Co-operation Scheme grant led by Rosemary Mardling and Rainer Spurzem. CF is grateful for support from Ralf Klessen during the initial steps of this project. CF acknowledges financial support from the International Max Planck Research School for Astronomy and Cosmic Physics (IMPRS-A) and the Heidelberg Graduate School of Fundamental Physics (HGSFP: funded by the Excellence Initiative of the German Research Foundation DFG GSC 129/1). The figures were produced

with SPLASH (Price 2007), using the new giza/cairo backend written by James Wetter. Calculations using PHANTOM were run using the NCI supercomputing facilities and on a dedicated node of the Monash Sun Grid, ably managed by Philip Chan and the e-research centre at Monash without whom this research would not have been possible. The FLASH simulations used computational resources from the HLRB-II project grant pr32lo at the Leibniz Rechenzentrum Garching. The software used in this work was in part developed by the DOE-supported ASC/Alliance Center for Astrophysical Thermonuclear Flashes at the University of Chicago.

REFERENCES

Ballesteros-Paredes J., Gazol A., Kim J., Klessen R. S., Jappsen A.-K., Tejero E., 2006, ApJ, 637, 384
Ballesteros-Paredes J., Klessen R. S., Mac Low M.-M., Vazquez-Semadeni E., 2007, in Reipurth B., Jewitt D., Keil K., eds, Protostars and Planets V. Univ. Arizona Press, Tucson, AZ, p. 63
Bartosch L., 2001, Int. J. Modern Phys. C, 12, 851
Beetz C., Schwarz C., Dreher J., Grauer R., 2008, Phys. Lett. A, 372, 3037
Berger M. J., Colella P., 1989, J. Comput. Phys., 82, 64
Boldyrev S., 2002, ApJ, 569, 841
Calder A. C. et al., 2002, ApJ, 143, 201
Colella P., Woodward P. R., 1984, J. Comput. Phys., 54, 174
Dib S., Brandenburg A., Kim J., Gopinathan M., André P., 2008, ApJ, 678, L105
Dimonte G. et al., 2004, Phys. Fluids, 16, 1668
Dubey A. et al., 2008, in Pogorelov N. V., Audit E., Zank G. P., eds, ASP Conf. Ser. Vol. 385, Numerical Modelling of Space Plasma Flows. Astron. Soc. Pac., San Francisco, p. 145
Elmegreen B. G., 2008, ApJ, 672, 1006
Elmegreen B. G., Falgarone E., 1996, ApJ, 471, 816
Elmegreen B. G., Scalo J., 2004, ARA&A, 42, 211
Eswaran V., Pope S. B., 1988, Comput. Fluids, 16, 257
Falgarone E., Lis D. C., Phillips T. G., Pouquet A., Porter D. H., Woodward P. R., 1994, ApJ, 436, 728
Federrath C., Klessen R. S., Schmidt W., 2008, ApJ, 688, L79
Federrath C., Klessen R. S., Schmidt W., 2009, ApJ, 692, 364
Federrath C., Duval J., Klessen R. S., Schmidt W., Mac Low M.-M., 2010, A&A, 512, 81
Fryxell B. et al., 2000, ApJ, 131, 273
Heitmann K., Ricker P. M., Warren M. S., Habib S., 2005, ApJ, 160, 28
Hennebelle P., Chabrier G., 2008, ApJ, 684, 395
Heyer M. H., Brunt C. M., 2004, ApJ, 615, L45
Hily-Blant P., Falgarone E., Pety J., 2008, A&A, 481, 367
Kitsionas S. et al., 2009, A&A, 508, 541
Klessen R. S., 2000, ApJ, 535, 869
Klessen R. S., Heitsch F., Mac Low M.-M., 2000, ApJ, 535, 887
Kolmogorov A., 1941, Doklady Akademi Nauk SSSR, 30, 301
Kritsuk A. G., Norman M. L., Padoan P., Wagner R., 2007a, ApJ, 665, 416
Kritsuk A. G., Padoan P., Wagner R., Norman M. L., 2007b, in Shaikh D., Zank G. P., eds, AIP Conf. Ser. Vol. 932, Turbulence and Nonlinear Processes in Astrophysical Plasmas. Am. Inst. Phys., New York, p. 393
Krumholz M. R., McKee C. F., 2005, ApJ, 630, 250
Larson R. B., 1981, MNRAS, 194, 809
Lemaster M. N., Stone J. M., 2008, ApJ, 682, L97
McKee C. F., Ostriker E. C., 2007, ARA&A, 45, 565
Mac Low M., Klessen R. S., 2004, Rev. Modern Phys., 76, 125
Mac Low M., Klessen R. S., Burkert A., Smith M. D., 1998, Phys. Rev. Lett., 80, 2754
Monaghan J. J., 1989, J. Comput. Phys., 82, 1
Monaghan J. J., 1992, ARA&A, 30, 543
Monaghan J. J., 1997, J. Comput. Phys., 136, 298
Monaghan J. J., 2005, Rep. Progress Phys., 68, 1703
Morris J. P., Monaghan J. J., 1997, J. Comput. Phys., 136, 41
Nordlund Å.K., Padoan P., 1999, in Franco J., Carraminana A., eds, Proc. 2nd Guillermo Haro Conf. Interstellar Turbulence. Cambridge Univ. Press, Cambridge, p. 218
Padoan P., 1995, MNRAS, 277, 377
Padoan P., Nordlund Å., 2002, ApJ, 576, 870
Padoan P., Nordlund A., Jones B. J. T., 1997, MNRAS, 288, 145
Padoan P., Nordlund Å., Kritsuk A. G., Norman M. L., Li P. S., 2007, ApJ, 661, 972
Passot T., Vázquez-Semadeni E., 1998, Phys. Rev. E, 58, 4501
Porter D. H., Woodward P. R., Pouquet A., 1998, Phys. Fluids, 10, 237
Price D. J., 2004, PhD thesis, Univ. of Cambridge, preprint (astro-ph/0507472)
Price D. J., 2007, Publ. Astron. Soc. Australia, 24, 159
Price D. J., 2010, MNRAS, 401, 1475
Price D. J., Bate M. R., 2008, MNRAS, 385, 1820
Price D. J., Monaghan J. J., 2004, MNRAS, 348, 139
Price D. J., Monaghan J. J., 2007, MNRAS, 374, 1347
Salpeter E. E., 1955, ApJ, 121, 161
Schmidt W., Hillebrandt W., Niemeyer J. C., 2006, Comput. Fluids, 35, 353
Schmidt W., Federrath C., Klessen R., 2008, Phys. Rev. Lett., 101, 194505
Schmidt W., Federrath C., Hupp M., Kern S., Niemeyer J. C., 2009, A&A, 494, 127
She Z.-S., Leveque E., 1994, Phys. Rev. Lett., 72, 336
Solomon P. M., Rivolo A. R., Barrett J., Yahil A., 1987, ApJ, 319, 730
Vazquez-Semadeni E., 1994, ApJ, 423, 681
Vázquez-Semadeni E., Ballesteros-Paredes J., Klessen R. S., 2003, ApJ, 585, L131
Zuckerman B., Evans N. J. II, 1974, ApJ, 192, L149

APPENDIX A: EFFECT OF β-VISCOSITY IN THE SPH CALCULATIONS

Fig. A1 shows the results of three 128^3 particle SPH calculations after 2 dynamical times using $\beta_{\rm visc} = 1$ (left), $\beta_{\rm visc} = 2$ (middle) and $\beta_{\rm visc} = 4$ (right) in the SPH artificial viscosity term (9)–(10). At this high Mach number, using $\beta_{\rm visc} < 4$ means that particle interpenetration can occur at the shock fronts (i.e. particles overshoot the shock), resulting in excess noise in the density field compared to the grid-based results and compared to the SPH results at higher $\beta_{\rm visc}$. In particular, the shocks appear much *sharper* and well defined at higher $\beta_{\rm visc}$, somewhat counter-intuitively since we are adding more viscosity. Using $\beta_{\rm visc} = 4$ shows good agreement with the grid-based shock structures (cf. Figs 3 and 4).

APPENDIX B: EFFECT OF THE FITTING RANGE ON THE MEASURED STRUCTURE FUNCTION SLOPE

The best-fitting structure function slopes, ζ_p, computed from a least-squares fit to the transverse velocity- and density-weighted structure functions shown in Fig. 13, are shown in Fig. B1 as a function of

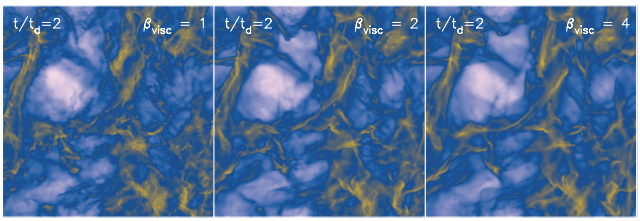

Figure A1. Effect of β-viscosity in the SPH calculations. From left to right: column density at $t/t_{\rm d} = 2$ in 128^3 SPH calculations using $\beta_{\rm visc} = 1$, $\beta_{\rm visc} = 2$ and $\beta_{\rm visc} = 4$. With $\beta_{\rm visc} \lesssim 2$ particle penetration occurs in the shocks at these high Mach numbers, causing them to lose definition.

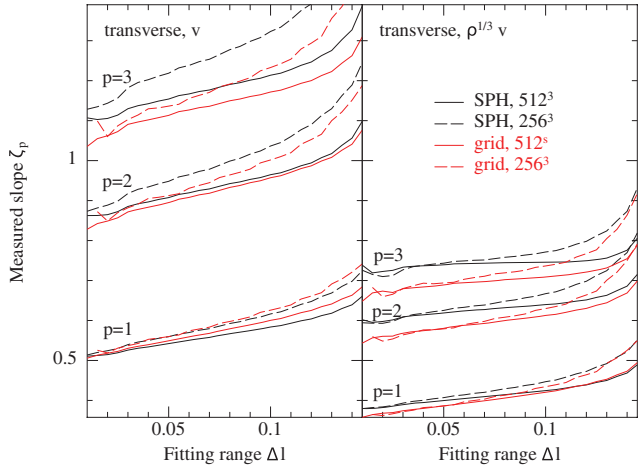

Figure B1. The dependence of the measured structure function slope ζ_p on the range in scales (lag) over which the least-squares fit to the time-averaged structure function is performed, where $\Delta l \equiv l_{\rm max} - l_{\rm min}$ and we have used a fixed $l_{\rm max} = 0.15$. The measured slope, shown for the three lowest order structure functions ($p = 1, 2, 3$) shows a strong dependence on the adopted fitting range, particularly for the velocity structure functions (left-hand panel) and to a lesser extent for the density-weighted ($\rho^{1/3}\boldsymbol{v}$) versions (right-hand panel). Thus, although the slopes appear to converge in individual codes for a fixed Δl, there remains a strong dependence on Δl, indicating that at a scaling range of constant ζ_p is not resolved in either code at the resolutions employed.

the range in the lag $\Delta l \equiv l_{\rm max} - l_{\rm min}$ used to perform the fitting. To produce the figure, we initially adopted a fixed $l_{\rm max} = 0.15$, based on visual inspection of Fig. 12 for the transverse case, and performed the fit down to $l_{\rm min} = l_{\rm max} - \Delta l$, plotting the resulting slope as a function of Δl. The results show a strong steepening of the measured slope as the fitting range is increased, indicating that the slope is not well fitted by a single power law. The $\rho^{1/3}$-weighted structure functions (right-hand panel) show a weaker dependence on Δl than for the pure velocity equivalents (left-hand panel), though the results from the two codes even in this case do not show convergence with each other. Convergence in each individual code is only obtained if a relatively short fitting range $\Delta l \lesssim 0.05$ is adopted, but it is clear that the converged value will nevertheless change if a different Δl is used. Neither can it be asserted that the adopted Δl should be changed with resolution, since it is not clear that any scaling range has been resolved even at the highest resolution adopted in either code (making the 'correct' choice $\Delta l = 0$ for the numerical resolutions tested in this code comparison).

This paper has been typeset from a TEX/LATEX file prepared by the author.

© 2010 The Authors. Journal compilation © 2010 RAS, MNRAS **406,** 1659–1674